Available online at www.sciencedirect.com
ScienceDirect
Trans. Nonferrous Met. Soc. China 34(2024) 2381−2392
Transactions of Nonferrous Metals Society of China
www.tnmsc.cn

Electrochemical behavior of $MgCl_2$ and co-deposition mechanisms of Mg and Sr in $SrCl_2$−KCl−$MgCl_2$ melt

Jia ZHAO[1,2,3], Yi-hang YAN[3], Hao ZHANG[3], Hua-yang GAO[3], Ye ZHANG[1,2,3], Gui-min LU[1,2]

1. National Engineering Research Center for Integrated Utilization of Salt Lake Resource, East China University of Science and Technology, Shanghai 200237, China;
2. Joint International Laboratory for Potassium and Lithium Strategic Resources, East China University of Science and Technology, Shanghai 200237, China;
3. School of Chemical Engineering, East China University of Science and Technology, Shanghai 200237, China

Received 12 January 2023; accepted 15 August 2023

Abstract: The electrochemical behavior of $MgCl_2$ and the co-deposition mechanisms of Mg and Sr in the $SrCl_2$−KCl eutectic system were evaluated using various electrochemical techniques, including cyclic voltammetry (CV), square wave voltammetry (SWV), and open-circuit potential (OCP) analysis. It was observed the Mg(II) reduction on the tungsten electrode in $SrCl_2$−KCl melt occurred in a single-step process involving the transfer of two electrons, exhibiting a quasi-reversible mode. The electrochemical co-deposition of Mg and Sr in the $SrCl_2$−KCl−$MgCl_2$ melt involved the formation of two types of Mg−Sr intermetallic compounds. The evolution in the co-deposition mechanism of the nucleation type with changing overpotential was explored through chronoamperometry (CA). It is shown that the nucleation pattern on the electrode surface was depended on the substrate materials and the electrode reaction products. Early-stage nucleation was attributed to Mg(II) reduction under all overpotential conditions. With the co-deposition of Mg and Sr, Mg(II) was reduced to form the Mg nucleus on the electrode surface, followed by underpotential deposition of Sr(II) on the Mg surface accompanied by Mg deposition simultaneously. Additionally, increasing $MgCl_2$ concentration in the $SrCl_2$−KCl melt resulted in a higher current density during the Mg−Sr co-deposition process.
Key words: $MgCl_2$; electrochemical behavior; diffusion coefficient; nucleation mechanism; co-deposition

1 Introduction

As the “green engineering material of the 21st century” [1], magnesium (Mg) metal exhibits numerous excellent properties, including low density, recyclability, high thermal conductivity, large hydrogen storage capacity, and exceptional damping performance [2]. Consequently, Mg and its alloys are being increasingly utilized in various industries, such as automotive [3], aerospace [4], the 3C industry (computers, communications, and consumer electronics) [5], and energy storage [6]. Given the global shortage of energy and resources and the rapid development in aerospace, national defense, military, and other sectors, high-performance, lightweight magnesium alloys hold significant importance and garner considerable attention.

Strontium (Sr) is recognized as a beneficial addition to magnesium alloys. The homogeneous distribution of Sr dispersoids in the AZ91 substrate improves alloy hardness and facilitates grain refinement [7]. Tensile and creep resistance tests conducted on Mg−Al−Sr alloy have demonstrated the positive effect of Sr addition on magnesium

Corresponding author: Ye ZHANG, Tel: +86-21-64250981, E-mail: zhangye@ecust.edu.cn;
Gui-min LU, Tel: +86-21-64252173, E-mail: gmlu@ecust.edu.cn
DOI: 10.1016/S1003-6326(24)66548-9

alloys [8]. Based on impregnation tests and electrochemical measurements, the simultaneous incorporation of Sr and Sn to the Mg−Zr−Ca alloy has been found to enhance corrosion resistance [9]. YANG et al [10] investigated the effect of Sr addition on the Mg alloy's properties, revealing that 0.1 wt.% of Sr effectively refined the grain structure of Mg−3.8Zn−2.2Ca alloy and improved its tensile properties. Moreover, the addition of a small amount of Sr to the AZ61−0.7Si alloy leads to grain refinement and modification of the Mg_2Si phase, resulting in a remarkable improvement in the tensile and creep properties [11].

The Mg alloy preparation generally involves vacuum metallurgy and molten salt electrolysis. Vacuum metallurgy, as a traditional technique, suffers from several demerits, such as long process durations, composition segregation, and high energy consumption [12]. In contrast, molten salt electrolysis offers short processing time, low costs, and homogeneous product composition [13,14]. It has been successfully applied to various Mg-containing alloys, including Mg−Li alloys, Mg−Al alloys, Mg−Cu alloys, and Mg−La alloys. ZHANG et al [15] investigated the electrochemical formation of Mg−Li alloys in the LiCl−KCl molten salt system. They prepared Mg−Li−Al [16] and Mg−Li−Zn [17] alloys using the electrochemical co-deposition method. It is found that Mg−Li−Al alloys can be yielded through the under-potential deposition of Li on pre-deposited liquid Mg−Al alloy. As for Mg−Li−Zn alloy, CP measurements demonstrated that Mg, Li, and Zn co-deposited at current densities lower than −0.78 A/cm^2 in LiCl−KCl−$MgCl_2$ (8 wt.%)−$ZnCl_2$ (1 wt.%) molten salt system. LI et al [18] investigated the electrochemical behavior of Mg(II) and Al(III) in the LiCl−KCl melt for Mg−Al alloy preparation using potentiostatic electrolysis. As the over-potential increased, Al tended to segregate at the grain boundaries, with a decrease in Al content in the Mg−Al alloy. CHEN et al [19] studied the electrochemical formation mechanism of Mg−Cu alloys in LiCl−KCl eutectic mixture and obtained $MgCu_2$ and Mg_2Cu phases. WANG et al [20] explored the effect of electrolyte composition on the Mg−La alloys, and achieved a current efficiency of >90% using electrolyte composition of KCl (65 wt.%), $MgCl_2$ (20−15 wt.%), and $LaCl_3$ (15−20 wt.%). Overall, molten salt electrolysis shows promising application prospects for alloy preparation.

Electrochemical studies on the preparation of Mg−Sr alloy through molten salt electrolysis have been conducted [21]. However, limited information is available regarding Mg(II) electrochemical properties and Mg−Sr co-deposition mechanism in the molten salt system, which are crucial for electrolysis preparation of Mg−Sr alloy. Therefore, it is urgent to conduct related research to enhance the understanding of Mg−Sr electrolytic preparation. This work aims to explore the electrochemical behavior of Mg(II) and the Mg−Sr co-deposition mechanism in the $SrCl_2$−KCl molten salt system. The reduction mechanism of Mg(II), the nucleation mode, and the Mg−Sr co-deposition process are thoroughly investigated to provide guidance for the industrial preparation of the Mg−Sr alloy through molten salt electrolysis.

2 Experimental

2.1 Materials

KCl (>99.0%, Aladdin), $SrCl_2$ (>99.0%, Diper), and $MgCl_2$ (>99.0%, Aladdin) were subjected to vacuum drying for 20 h at a temperature of 473 K to eliminate residual moisture and then stored in the glove-box (Mikrouna) with oxygen and water levels below 0.1×10^{-5} wt.%. The eutectic composition of $SrCl_2$−KCl (42.7 mol.% and 57.3 mol.%) was used in each experiment, and anhydrous $MgCl_2$ was introduced into the system as the Mg(II) source. Figure 1 shows the detailed schematic diagram of the electrochemical experiment apparatus. Both working electrode and reference electrode were tungsten wires (d=1 mm, 99.99%), while the auxiliary electrode was a spectral pure graphite rod (d=6 mm).

2.2 Experimental method

All the measurements for cyclic voltammetry (CV), square wave voltammetry (SWV), electrochemical impedance spectroscopy (EIS), open circuit potential (OCP), chronopotentiometry (CP), and chronamperometry (CA) were conducted using a Princeton 4000 electrochemical workstation (Ametek Group Co., American). The workstation was controlled by VersaStudio software package. The measurements were performed in a three-

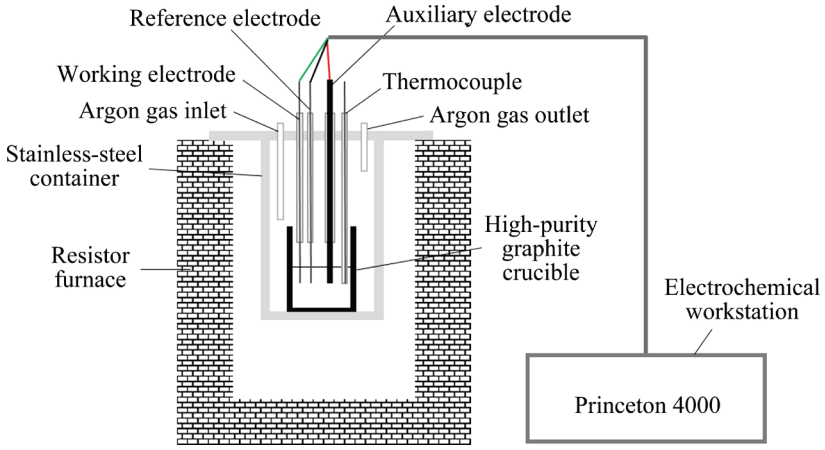

Fig. 1 Schematic diagram of electrochemical experiment apparatus

electrode system. Zview software was employed to process EIS data. Before the experiment, all electrodes were carefully polished with SiC paper and ultrasonically cleaned with ethanol (99%). The functioning area of the working area in the molten salt system was controlled using a homemade micro-positioning device, which was applied to controlling the working electrode depth. In the resistor furnace, a high-purity graphite crucible was used to hold the molten salt, sealed in the stainless-steel container, and heated. An inert atmosphere was maintained during the experiments by continuously supplying argon gas. The potentiostatic method at −1.8 V for 2 h was employed for the pre-electrolysis step to purify the melts. After $MgCl_2$ introduction, the melt was stirred by argon gas for 0.5 h to promote the homogeneity of the system. During the experiment, the system temperature was monitored using a thermocouple, which was enclosed in an Al_2O_3 tube. The temperature was controlled by the programmable device with an accuracy of ±1 K.

3 Results and discussion

3.1 Electrochemical behavior of Mg(II)

3.1.1 Cyclic voltammetry analysis

The CV curves obtained on the tungsten electrode in $SrCl_2$–KCl eutectic melts are shown in Fig. 2. The measurements were conducted before and after adding $MgCl_2$ at a temperature of 923 K. For the typical CV curve obtained in the pure $SrCl_2$–KCl melts, the cathodic peak D, occurring at approximately −2.30 V, was attributed to the Sr deposition on the electrode surface. In the reverse

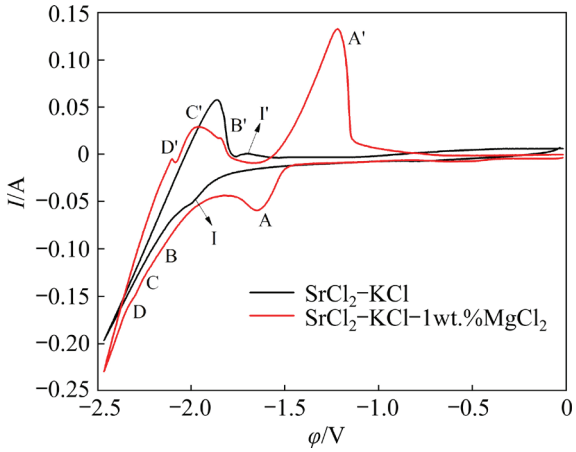

Fig. 2 CV curves on electrode W before and after addition of 1 wt.% $MgCl_2$ to $SrCl_2$–KCl system (S=0.322 cm^2; T=923 K; Scan rate: 0.1 V/s)

scan direction, the anodic peak D′ at −2.11 V corresponded to the Sr dissolution. Additionally, a small reduction peak I at −1.99 V, along with its corresponding oxidation peak I', was attributed to formation and dissolution of Sr−W intermetallics. Upon $MgCl_2$ addition, the redox couple of A/A′ corresponded to the deposition and dissolution of metallic Mg. Aside from couples A/A' and D/D', two distinct anodic peaks (B' and C') were observed, although their corresponding reduction signals were not apparent. The reduction−oxidation peak of the Sr−W alloy disappeared after the Mg(II) source introduction. This phenomenon can be explained by the Mg reduction occurring before the formation of Sr−W alloy. The preferentially formed Mg metal covered the electrode surface and inhibited the formation of Sr−W alloy.

The CV potential was adjusted to assign the redox coupling of these cathodic and anodic peaks,

as shown in Fig. 3. Six termination potentials were selected (−1.65, −2.05, −2.15, −2.25, −2.35 and −2.45 V). When the cathodic inversion potential was set as −1.65 V, only A/A′ redox couples appeared, with no other electrochemical signals present. This indicates that Mg metal could be directly deposited in a single step via the direct reduction of Mg(II) ions into Mg. Shifting the potential to −2.05 V did not result in apparent anodic peak in the positive-going scan, suggesting that −2.05 V was insufficient for the formation of Mg−Sr alloys. At −2.15 V, the B' peak can be observed, while the termination potential of −2.25 V was associated with the appearance of the C' peak. Consequently, the corresponding cathodic peaks of B (−2.10 V) and C (−2.20 V) were determined. These peaks represent the formations of Mg−Sr intermetallic compounds. The B' and C' peaks can be attributed to Mg dissolution into the melts as Mg(II), in conjunction with the decomposition of Mg−Sr intermetallic compounds. Finally, adjusting the potential to −2.35 and −2.45 V allowed for the observation of all peaks within the electrochemical window.

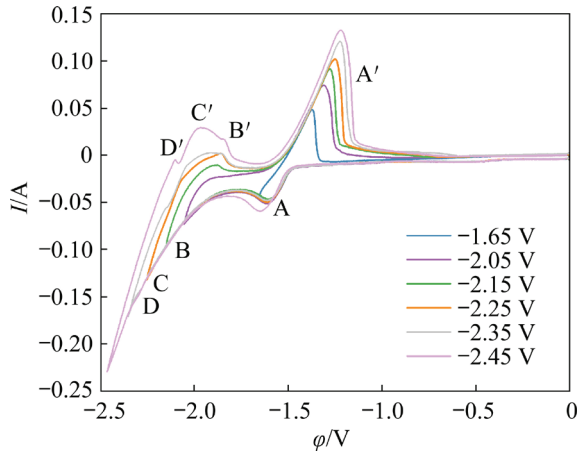

Fig. 3 CV curves at tungsten electrode (S=0.322 cm^2) of $SrCl_2$−KCl−$MgCl_2$ molten salt systems at different inversion potentials (Scan rate: 0.1 V/s)

3.1.2 Square-wave voltammetry analysis

SWV is a powerful technique utilized in the determination of electron transfer numbers for electrochemical reactions. Equation (1) establishes the correlation among the half-peak width ($W_{1/2}$), the number of electron transfer, and temperature:

$$W_{1/2}=3.5RT/(nF) \quad (1)$$

where R corresponds to the molar gas constant, T symbolizes the thermodynamic temperature, n represents the number of exchanged electrons, and F represents Faraday's constant.

Figure 4 shows the SWV results for the $MgCl_2$ reduction in the $SrCl_2$−KCl molten salts on a tungsten electrode at a temperature of 923 K. In agreement with the CV findings, only one reduction peak was observed within the electrochemical window. The presence of an asymmetrical shape in the reduction peak can be due to the nucleation overpotential of magnesium on the tungsten electrode. To ensure the accuracy, the half-peak width was determined using the left peak width to account for the nucleation effect. According to Eq. (1), n was deduced as 1.94, indicating that Mg(II) electrodeposition on the tungsten electrode in the $SrCl_2$−KCl molten salt system occurred in a single-step process involving the transfer of two electrons.

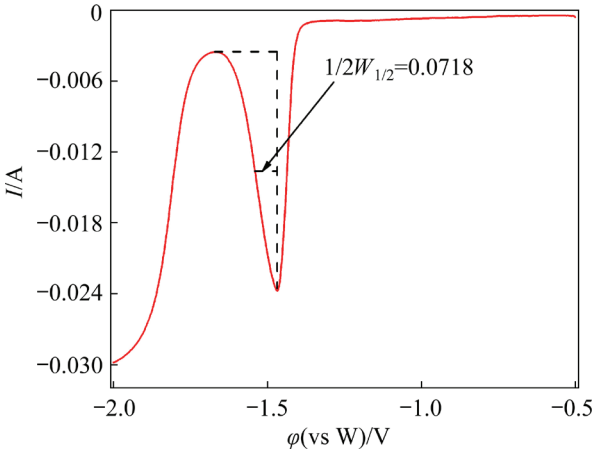

Fig. 4 Square-wave voltammograms for Mg(II) reduction on tungsten electrode (Pulse height: 25 mV; Step height: 2 mV; Frequency: 10 Hz; T=923 K)

3.1.3 Electrochemical impedance spectroscopy analysis

The EIS was employed to understand the electrolyte resistance, revealing the IR drop of the $SrCl_2$−KCl−1wt.%$MgCl_2$ system. Figure 5 displays the Nyquist plots for $SrCl_2$−KCl−1wt.%$MgCl_2$ melts on a tungsten electrode at a temperature of 923 K. The frequency ranged from 2000 to 1 Hz with a potential amplitude of 10 mV. The curve showed an remarkable linear relationship with slopes of 0.98 when the frequency was below 400 Hz. It is indicated that impedance processes accompany the mass transport of the species. The inset graph in Fig. 5 shows the equivalent circuit of

the electrochemical cell required for analyzing impedance spectra. In this circuit, R_s denotes the solution resistance, C_{dl} denotes the double-layer capacitance, R_{ct} represents the charge transfer resistance on the electrode surface, while CPE, previously adopted in the molten salt system by YOON and PHONGIKAROON [22] and YIN et al [23], describes diffusion-related resistance. The consistency between the measured and the fitting results confirms the accuracy of the findings. Subsequently, the initial value was determined by instant fitting and then assigned to respective element in the equivalent circuit. The fitted data yielded a resistance value of 1.146 Ω for the $SrCl_2$−KCl−$MgCl_2$ melt with 0.3% of error margin.

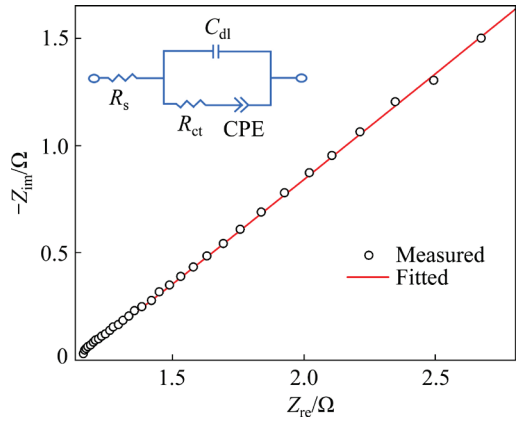

Fig. 5 Measured and fitted Nyquist plots for $SrCl_2$−KCl−1wt.%$MgCl_2$ melts on tungsten electrode (S=0.322 cm^2) at 923 K (Inset graph illustrates the equivalent circuit of the electrochemical cell)

Furthermore, the Mg(II)/Mg(0) reversibility was evaluated over a wide range of scan rates from 0.05 to 0.50 V/s. Figure 6 shows the corresponding results after potential compensation based on the electrolyte resistance, which can reduce experimental artifacts. It is observed that the cathodic potential shifted slightly to negative values as the scan rate increased, accompanied by a successive increase in the cathodic current, implying that the Mg(II) reduction was not completely reversible.

The Mg(II)/Mg(0) reversibility was discussed in-depth using the diagnostic parameter (Λ) [24], as given in Eq. (2):

$$\Lambda = \frac{k^0}{[DnF/(RT)]^{1/2}} \frac{1}{v^{1/2}} \tag{2}$$

where D is the diffusion coefficient equal to

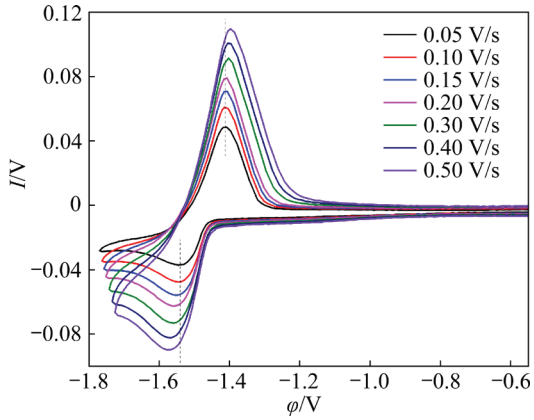

Fig. 6 CV curves for Mg(II) reduction after correcting ohmic resistance drop in $SrCl_2$−KCl−$MgCl_2$ melts over scan rate ranging from 0.05 to 0.50 V/s

9.46×10^{-6} cm^2/s; v denotes the potential scanning rate (V/s). For the reversible reaction, $\Lambda \geq 15$. For the quasi-reversible reaction, $10^{-2(1+\alpha)} \leq \Lambda < 15$. For the irreversible reaction, $\Lambda < 10^{-2(1+\alpha)}$. α represents the transfer coefficient for Mg(II)/Mg(0), equal to 0.204. k^0 (cm/s) is derived from the difference between the anodic and cathodic peak potentials, as given in Eq. (3):

$$k^0 = 2.18\left(\frac{Dn\alpha Fv}{RT}\right)^{0.5} \exp\left(\frac{\alpha^2 nF}{RT}(\varphi_p^c - \varphi_p^a)\right) \tag{3}$$

where φ_p^c and φ_p^a are the cathodic and anodic peak potentials, respectively.

Table 1 lists the value of k^0 and Λ at various scanning rates. As the scanning rate increases, k^0 shows a similar trend while Λ decreases slightly. However, the variations in Λ values are negligible in relation to the quasi-reversible reaction criteria ($0.004 \leq \Lambda < 15$). Therefore, Mg(II) reduction on the tungsten electrode is considered a quasi-reversible process.

Table 1 $\varphi_p^c - \varphi_p^a$, k^0, and Λ at various scanning rates for $SrCl_2$−KCl−$MgCl_2$ melts on tungsten electrode

v/(V·s^{-1})	$(\varphi_p^c - \varphi_p^a)$/ V	k^0/(cm·s^{-1})	Λ
0.05	−0.1301	0.0030	0.8593
0.10	−0.1340	0.0042	0.8558
0.15	−0.1422	0.0051	0.8485
0.20	−0.1495	0.0058	0.8420
0.30	−0.1588	0.0070	0.8339
0.40	−0.1678	0.0081	0.8261
0.50	−0.1772	0.0089	0.8180

3.1.4 Open-circuit chronopotentiometry analysis

OCP, which describes the evolution of the potential over time, is an appropriate electrochemical technique for studying the formation and dissolution of alloys [25]. Figure 7 illustrates the potential evolution of the working electrode against the reference electrode over time in the $MgCl_2$−$SrCl_2$−KCl molten salt system at a temperature of 923 K. Firstly, a continuous potential pulse of −2.55 V was applied for 7 s between the working electrode and the counter electrode. During this period, a thin layer of the specimen was deposited on the working electrode surface. Subsequently, the potential stepped up and exhibited four plateaus, namely D (−2.11 V), C (−2.01 V), B (−1.95 V), and A (−1.38 V), which is consistent with CV results. Plateaus D and A were attributed to the presence of Sr and Mg, respectively, deposited on the electrode surface. In other words, the equilibrium electrode potentials of Sr(II)/Sr and Mg(II)/Mg with respect to tungsten in the $MgCl_2$−$SrCl_2$−KCl melts were −2.11 and −1.38 V, respectively. The plateaus B and C corresponded to the formation of Mg−Sr alloys. Plateau B represented a two-phase coexisting state of an alloy with Mg, while plateau C represented another alloy with Sr. When elapsed time exceeded 40 s, the potential rose rapidly in that the deposits on the working electrode surface were thoroughly consumed.

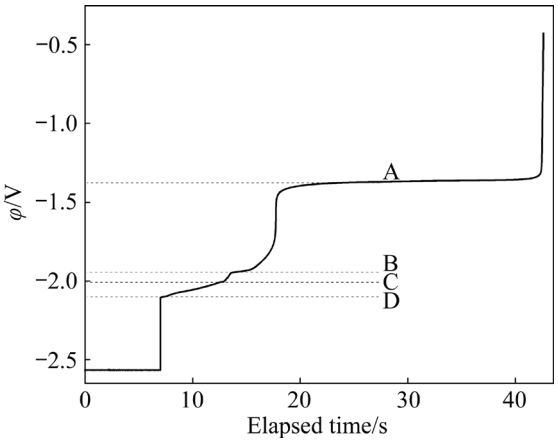

Fig. 7 Potential evolution of working electrode against reference electrode over time in $SrCl_2$−KCl eutectic melts containing 1 wt.% $MgCl_2$ at 923 K

3.1.5 Diffusion coefficient and activation energy

Figure 8 depicts CPs recorded on the tungsten electrode for $MgCl_2$ in $SrCl_2$−KCl eutectic melts at different current intensities. A potential plateau appeared at around −1.50 V, which corresponded to the Mg(II) reduction into Mg metal, and the duration of this plateau decreased with the applied current. The potential shifted negatively rapidly and converged on another plateau, corresponding to the reduction of the Mg−Sr alloy and the Sr deposition. As evidenced by the CV results, the potential for the reduction of the Mg−Sr alloy was close to that of Sr deposition. Therefore, the plateau associated with the Mg−Sr alloy reduction was obscured by that corresponding to Sr reduction.

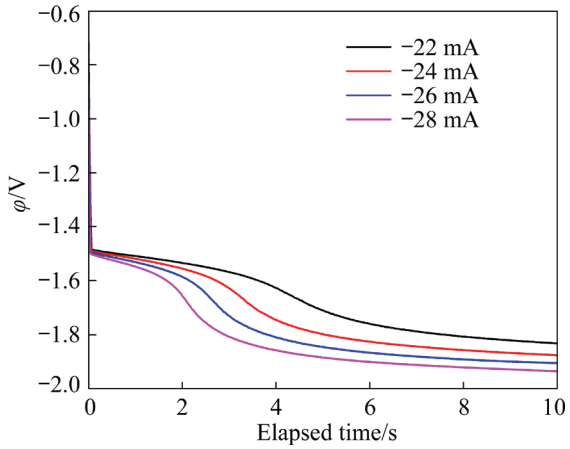

Fig. 8 Typical CPs for $SrCl_2$−KCl−$MgCl_2$ melt on tungsten electrode at different current (T=923 K; Electrode area: 0.322 cm^2)

The Laity method [26] was adopted to ascertain the transition time for magnesium reduction. Figure 9 illustrates the linear evolution for I versus $\tau^{-1/2}$ at different temperatures ranging 873−948 K. This linear relationship indicates the suitability of Sand's equation, deduced for mass transfer processes, in evaluating the diffusion coefficient of Mg(II) in $SrCl_2$−KCl melt. Table 2 gives the diffusion coefficients of Mg(II) at different temperatures, determined by Eq. (4):

$$I\tau^{1/2}=0.5nFC_0S\pi^{1/2}D^{1/2} \quad (4)$$

where I represents the applied current (A), τ represents the transition time (s), C_0 represents the bulk concentration of Mg(II) in the melts (mol/mL), and S denotes the surface area of the working electrode (cm^2).

Figure 10 shows the evolution of natural logarithm of the diffusion coefficient as a function of temperature, with diffusion activation energy of 28.73 kJ/mol deduced from the slope of the plot.

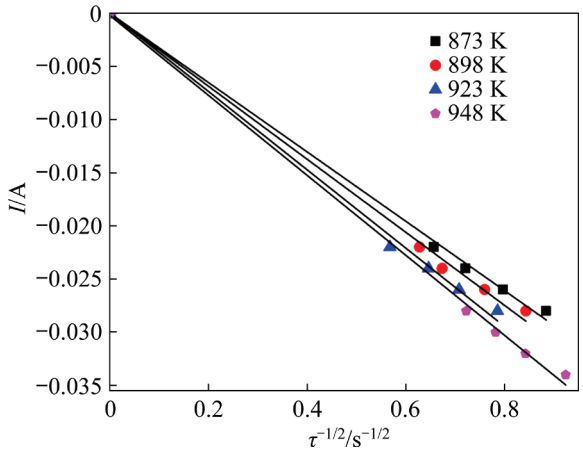

Fig. 9 Linear evolution of I versus $\tau^{-1/2}$ at different temperatures ranging from 873 to 948 K

Table 2 Diffusion coefficients of Mg(II) in molten $SrCl_2$–KCl eutectic salt at different temperatures of 873–948 K

T/K	D/(cm^2·s^{-1})
873	7.49×10^{-6}
898	8.30×10^{-6}
923	9.46×10^{-6}
948	1.01×10^{-5}

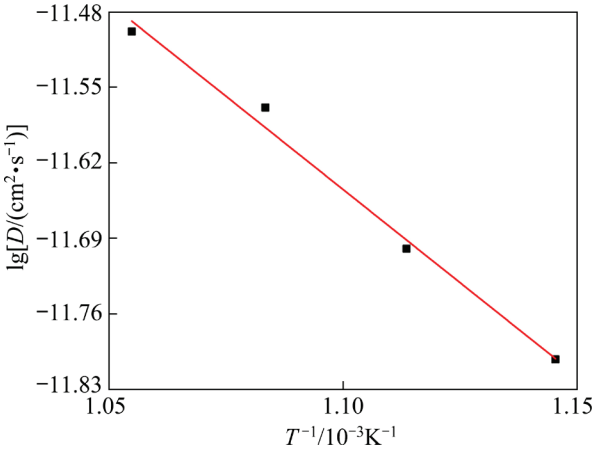

Fig. 10 Dependence of ln D on $1/T$ based on chronopotentiograms

3.2 Co-deposition mechanism for Mg–Sr alloy

3.2.1 Chronoamperometry and nucleation mechanism

CA is an electrochemical measurement technique that records the current evolution over time under a constant potential pulse. CA methods are widely used in the molten salt field to analyze the nucleation mechanism of metal ions on the electrode substrate [27–29], as its initial response of the current in I–t curve reflects the characteristic of nucleus formation. Figure 11 depicts the dependence of current with time on the tungsten electrode in the $SrCl_2$–KCl–$MgCl_2$ melts under different applied potentials. In the initial stage, the current increased rapidly to its maximum value, signifying the formation and growth of Mg and Sr nuclei. Subsequently, the current gradually decreased due to diffusion control. Moreover, the higher the overpotential, the greater the current value.

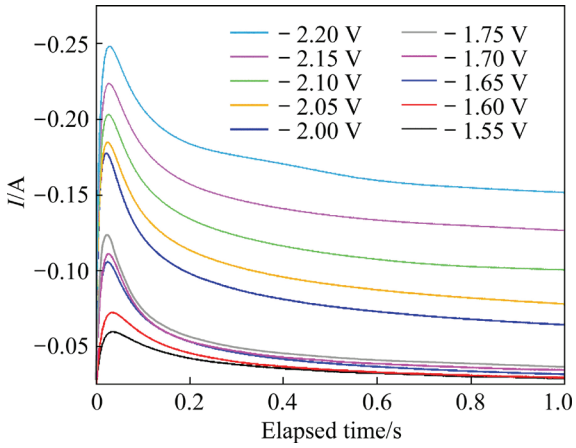

Fig. 11 Chronoamperometry I–t curves for deposition of Mg on tungsten electrode at temperature of 923 K

According to the CA experiments data, SCHARIFKER and HILLS [30] developed a non-dimensional model to reveal the nucleation mechanism of metal ions on the electrode surface. The detailed expressions are shown in Eqs. (5) and (6).

For instantaneous nucleation:

$$\left(\frac{I}{I_m}\right)^2 = 1.9542\left(\frac{t_m}{t}\right)\left\{1-\exp\left[-1.2564\left(\frac{t}{t_m}\right)\right]\right\}^2 \quad (5)$$

For progressive nucleation:

$$\left(\frac{I}{I_m}\right)^2 = 1.2254\left(\frac{t_m}{t}\right)\left\{1-\exp\left[-2.3367\left(\frac{t}{t_m}\right)^2\right]\right\}^2 \quad (6)$$

where I and I_m represent current and peak current, respectively, t and t_m represent time and peak current time, respectively. In LiCl–KCl melts, the effect of overpotential on the nucleation mechanism of erbium [31], gadolinium [32], dysprosium [33], terbium [34], and yttrium [35] on the electrode

surface was investigated. It is consistently concluded that the nucleation mode remained unchanged regardless of overpotential. However, the overpotential range investigated in these studies was relatively limited. Therefore, in this study, a wider overpotential interval was considered to comprehensively understand the overpotential effect on the nucleation mechanism.

To gain insights into the nucleation mechanism of metal ions on the surface of the working electrode, Fig. 12 shows the comparison of the experimental data for various applied potentials with the instantaneous and progressive nucleation theoretical models, as presented in Eqs. (5) and (6). A series of CA measurements were performed under different overpotentials in the $SrCl_2$−KCl−$MgCl_2$ melts to investigate the evolution rule. According to the OCP experiment results, these overpotential scenarios involved the Mg deposition on the electrode surface (Fig. 12(a)) as well as the nucleation and growth of Mg and Sr on the substrates (Fig. 12(b)). Remarkably, regardless of the overpotentials, the nucleation mechanisms were consistent with the instantaneous nucleation model until t/t_m was about 1. Moreover, the further growth of instantaneously formed nuclei was sensitive to variations in overpotentials.

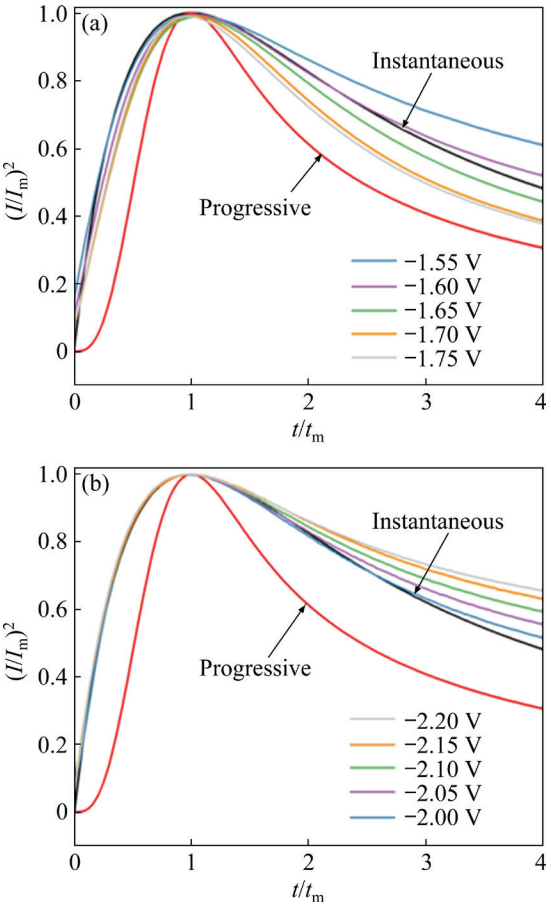

Fig. 12 Comparison of experimental data for various applied potentials deduced from I–t curves with instantaneous and progressive nucleation theoretical models: (a) From −1.55 to −1.75 V; (b) From −2.20 to −2.00 V

When t/t_m was greater than 1, the nucleation type for the magnesium reduction transitioned from instantaneous nucleation to progressive nucleation as the overpotential increased. This shift in nucleation type was a result of the varied overpotential-induced changes in the substrates occurring on the electrode surface over time. Specifically, the higher overpotential facilitated faster transformation into the magnesium substrate on the electrode surface, ultimately leading to differences in the nucleation patterns due to the contrasting crystal structures of magnesium and tungsten. Additionally, when the overpotential reached a level where the simultaneous deposition of Mg and Sr occurring on the electrode surface, the nucleation regime exhibited fluctuations but remained within the domain of instantaneous nucleation as t/t_m exceeded 1. Notably, this trend was opposite from the observations made under lower overpotential conditions. During the co-deposition of Mg and Sr, Mg(II) reduction occurred and resulted in the formation of Mg nucleus on the electrode surface, followed by an underpotential deposition of Sr(II) on Mg surface accompanied by Mg deposition simultaneously. Thus, early-stage nucleation primarily stemmed from Mg(II) reduction, irrespective of the specific overpotential conditions, leading to a consistent nucleation pattern. However, as time increased, strontium reduction also took place, leading to alterations in the electrode surface product. Consequently, these discrepancies in the deposited species brought about distinct nucleation pattern when compared to scenarios characterized by lower overpotential. Similarly, based on the Scharifker and Hills model, TYLKA et al [36] reported that the deposition of uranium (U) alone exhibited a progressive nucleation mode, while the addition of plutonium (Pu) shifted the nucleation mechanism to the instantaneous nucleation. This demonstrated that the characteristics of the electrode surface deposit would affect the nucleation mode. Accordingly, in the $SrCl_2$−KCl−$MgCl_2$ melt, the

nucleation of metal ions was dependent on both the electrode substrate and the composition of the deposited species.

3.2.2 Chronopotentiometry and co-deposition discussion

The co-deposition mechanism of Mg and Sr on tungsten electrodes in the $SrCl_2$−KCl system with different $MgCl_2$ concentrations at a temperature of 923 K was further investigated using the CPs method, as illustrated in Fig. 13. In the absence of $MgCl_2$ (Fig. 13(a)), a potential plateau was observed around −1.8 V for Sr reduction when a current of −20 mA (0.062 A/cm^2) was applied. This plateau shifted towards more negative potentials with increasing current density. In the presence of 1 wt.% $MgCl_2$ (Fig. 13(b)), same current density was applied to the working electrode, causing the potential to rapidly decrease to around −1.5 V. This potential shift corresponded to the deposition of Mg on the surface of the working electrode, as confirmed by voltammetry results. When the current density for Mg(II) approached the limiting diffusion current density, the potential plateau shifted towards more negative potentials, and Sr(II) in the melt started to gain electrons at approximately −1.7 V due to the formation of Mg−Sr alloy, signifying the co-deposition of Mg and Sr. When $MgCl_2$ concentration in the system increased to 5 wt.% (Fig. 13(c)), the reduction plateau resulting from Mg(II) shifted towards more negative potentials as the current increased. Sr was deposited on the electrode surface at a current of −70 mA (0.217 A/cm^2). As the $MgCl_2$ concentration reached 10 wt.% (Fig. 13(d)), the current required for Mg−Sr co-deposition increased to −200 mA (0.621 A/cm^2).

Consequently, an increase in current density leads to a cathodic shift of the deposition potential of Mg(II) and Sr(II) in the melt. Furthermore, increasing the concentration of Mg(II) enlarged the current density for Mg and Sr co-deposition. This implies that the regulation of Sr content within the Mg substrate can be achieved by adjusting the $MgCl_2$ concentration and applied current density. This conclusion is consistent with previous studies involving the preparation of Mg−La [20] and Mg−Pr [37] intermediate compounds by molten salt electrolysis.

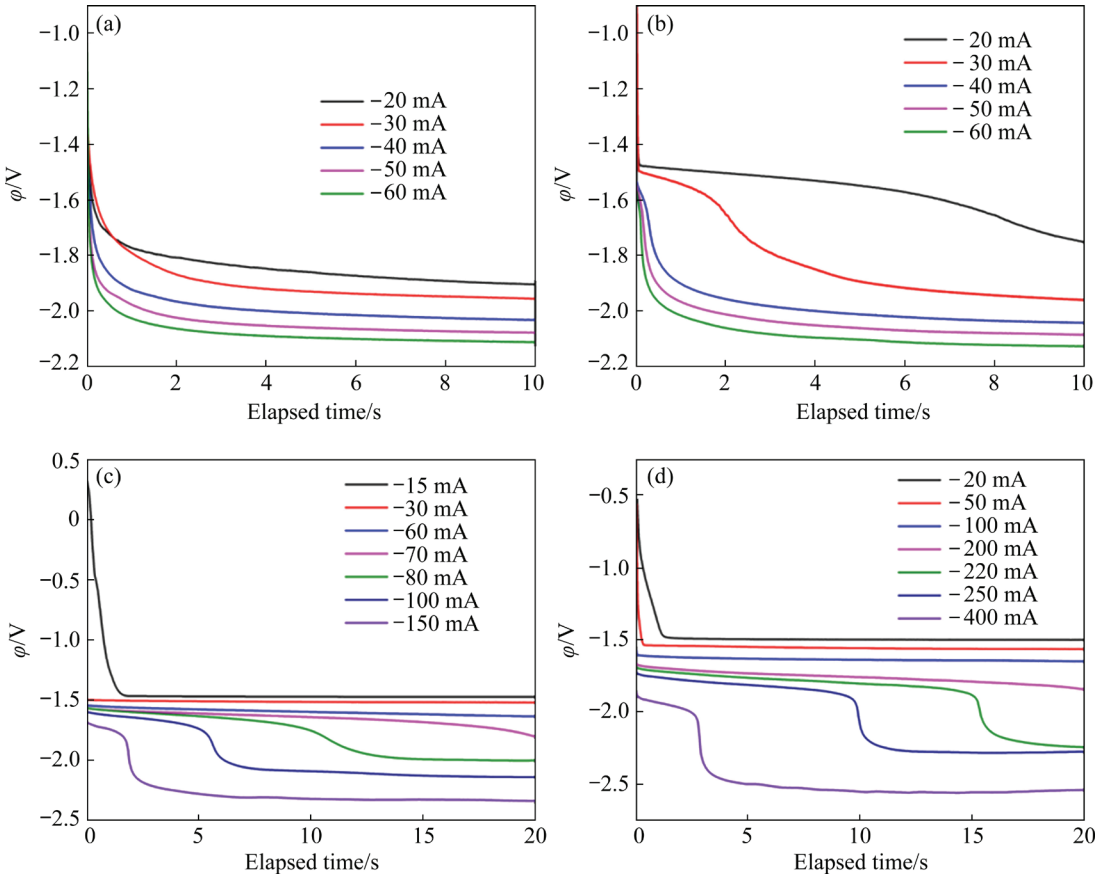

Fig. 13 Evolution of potential with time at different applied currents recorded by CP for $SrCl_2$−KCl system with different $MgCl_2$ contents at 923 K (S=0.322 cm^2): (a) 0% $MgCl_2$; (b) 1% $MgCl_2$; (c) 5% $MgCl_2$; (d) 10% $MgCl_2$

4 Conclusions

(1) The Mg(II) deposition on the tungsten electrode in the $SrCl_2$−KCl eutectic occurred in a single-step process involving the transfer of two electrons, resulting in the formation of two kinds of Mg−Sr intermetallic compounds. Electrochemical impedance spectroscopy (EIS) analysis indicated that the electrolyte resistance of $SrCl_2$−KCl−$MgCl_2$ (1 wt.%) system was measured to be 1.146 Ω at a temperature of 923 K. Moreover, the quasi-reversible mode of Mg(II) reduction on the tungsten electrode was confirmed through cyclic voltammetry measurements. Diffusion coefficient for Mg(II) within the $SrCl_2$−KCl eutectic was determined to be 9.46×10^{-6} cm^2/s at a temperature of 923 K, with an activation energy (E_a) of 28.73 kJ/mol.

(2) The nucleation mechanism governing the co-deposition of Mg and Sr was consistent with that observed for Mg during the early nucleation stages. However, a change in the nucleation pattern was subsequently observed due to the different products formed on the electrode surface resulting from the presence of Sr.

(3) The CPs analysis for $SrCl_2$−KCl eutectic with different $MgCl_2$ concentrations demonstrated that Sr content in the Mg substrate could be regulated by manipulating both the $MgCl_2$ concentration and the applied current density during the co-deposition process.

CRediT authorship contribution statement

Jia ZHAO: Conceptualization, Validation, Methodology; **Yi-hang YAN:** Data curation, Visualization; **Hao ZHANG:** Data curation, Investigation; **Hua-yang GAO:** Data curation, Visualization; **Ye ZHANG:** Conceptualization, Reviewing; **Gui-min LU:** Resources, Supervision.

Declaration of competing interest

The authors declare that they have no known competing financial interests or personal relationships that could have appeared to influence the work reported in this paper.

Acknowledgments

The authors acknowledge the financial support provided by the National Natural Science Foundation of China (No. U20A20147).

References

[1] YANG Hai-liang, WANG Xiao, NI Peng, LI Zhe-wen, LIU Hui-xia. Construction of high strain rate loading constitutive model and failure model and prediction of forming limit for LA103Z magnesium alloy [J]. Metals and Materials International, 2022, 28(8): 1938−1947.

[2] YANG Yan, XIONG Xiao-ming, CHEN Jing, PENG Xiao-dong, CHEN Dao-lun, PAN Fu-sheng. Research advances in magnesium and magnesium alloys worldwide in 2020 [J]. Journal of Magnesium and Alloys, 2021, 9(3): 705−747.

[3] KULEKCI M K. Magnesium and its alloys applications in automotive industry [J]. The International Journal of Advanced Manufacturing Technology, 2008, 39(9): 851−865.

[4] ZHANG Xue-song, CHEN Yong-jun, HU Jun-ling. Recent advances in the development of aerospace materials [J]. Progress in Aerospace Sciences, 2018, 97: 22−34.

[5] WU F, ZHANG S, TAO Z. Corrosion behavior of 3C magnesium alloys in simulated sweat solution [J]. Materials and Corrosion, 2011, 62(3): 234−239.

[6] CRIVELLO J C, DENYS R V, DORNHEIM M, FELDERHOFF M, GRANT D M, HUOT J, JENSEN T R, de JONGH P, LATROCHE M, WALKER G S, WEBB C J, YARTYS V A. Mg-based compounds for hydrogen and energy storage [J]. Applied Physics A, 2016, 122(2): 85.

[7] LEE S, LEE S H, KIM D H. Effect of Y, Sr, and Nd additions on the microstructure and microfracture mechanism of squeeze-cast AZ91-X magnesium alloys [J]. Metallurgical and Materials Transactions A, 1998, 29(4): 1221−1235.

[8] PEKGULERYUZ M O, BARIL E. Creep resistant magnesium diecasting alloys based on alkaline earth elements [J]. Materials Transactions, 2001, 42(7): 1258−1267.

[9] ZHANG Wen-jin, LI Mei-heng, CHEN Qian, HU Wang-yu, ZHANG Wen-mei, XIN Wang. Effects of Sr and Sn on microstructure and corrosion resistance of Mg−Zr−Ca magnesium alloy for biomedical applications [J]. Materials & Design, 2012, 39: 379−383.

[10] YANG M B, CHENG L, PAN F S. Comparison about effects of Sr, Zr and Ce additions on as cast microstructure and mechanical properties of Mg−3.8Zn−2.2Ca (wt.%) magnesium alloy [J]. International Journal of Cast Metals Research, 2010, 23(2): 111−118.

[11] YANG Ming-bo, SHEN Jia, BAI Liang, PAN Fu-sheng. Effects of Sr on the microstructure, tensile and creep properties of AZ61−0.7 Si magnesium alloy [J]. International Journal of Minerals, Metallurgy and Materials, 2009, 16(1): 89−95.

[12] ZHANG Mi-lin, CAO Peng, HAN Wei, YAN Yong-de, CHEN Li-jun. Preparation of Mg−Li−La alloys by electrolysis in molten salt [J]. Transactions of Nonferrous Metals Society of China, 2012, 22(1): 16−22.

[13] WU Xiao-bin, ZHU Zeng-li, HUI Kong, FAN You-qi, CHENG Si-wei, HUA Zhong-sheng. Electrochemical

reduction mechanism of Zn^{2+} in molten NaCl−KCl eutectic [J]. Transactions of Nonferrous Metals Society of China, 2022, 32(9): 3088−3098.

[14] RUI Yuan, CHENG Lu, WAN He-li, LI Shao-long, CHE Yu-si, HE Ji-lin and SONG Jian-xun. Effect of fluoride addition on electrochemical behaviors of V(III) in molten LiCl−KCl [J]. Transactions of Nonferrous Metals Society of China, 2022, 32(8): 2736−2745.

[15] ZHANG Mi-lin, CHEN Zeng, HAN Wei, LV Yan-zhuo, WANG Jun. Electrochemical formation and phase control of Mg−Li alloys [J]. Chinese Chemical Letters, 2007, 18(9): 1124−1128.

[16] YAN Yong-de, ZHANG Mi-lin, XUE Yun, HAN Wei, CAO Dian-xue, HE Li-yi. Electrochemical study of the codeposition of Mg−Li−Al alloys from LiCl−KCl−$MgCl_2$−$AlCl_3$ melts [J]. Journal of Applied Electrochemistry, 2009, 39(3): 455−461.

[17] YAN Yong-de, ZHANG Mi-lin, XUE Yun, HAN Wei, CAO Dian-xue, WEI Shu-quan. Study on the preparation of Mg−Li−Zn alloys by electrochemical codeposition from LiCl−KCl−$MgCl_2$−$ZnCl_2$ melts [J]. Electrochimica Acta, 2009, 54(12): 3387−3393.

[18] LI Shao-long, CHE Yu-si, LI Chen-yao, SHU Yong-chun, HE Ji-lin, YANG Bin, SONG Jian-xun. Study on the electrochemical behavior of Mg and Al ions in LiCl−KCl melt and preparation of Mg−Al alloy [J]. Journal of Magnesium and Alloys, 2022, 10(3): 721−729.

[19] CHEN Zeng, WANG Bei, LI Sheng-jun, LI Wei, WEI Chao-chao, JIA Xi-yang, ZHANG Wei-feng. Electrochemical formation and phase control of Mg−Cu alloys [J]. ChemElectroChem, 2016, 3(1): 165−171.

[20] WANG Shi-dong, LI Quan, YE Xiu-shen, SUN Qing-guo, WU Zhi-jian. Electrolytic preparation of Mg−La alloy in chloride molten salt: effect of electrolyte composition [J]. Rare Metal Materials and Engineering, 2015, 44(7): 1623−1628.

[21] SUN Xiu-yun, LU Gui-min, FAN Shu-di. Electrochemical mechanism of electrolysis codeposition of Mg−Sr alloy in molten salt [J]. Transactions of Nonferrous Metals Society of China, 2014, 24(5): 1629−1634.

[22] YOON D, PHONGIKAROON S. Electrochemical properties and analyses of $CeCl_3$ in LiCl−KCl eutectic salt [J]. Journal of the Electrochemical Society, 2015, 162(10): E237.

[23] YIN Tai-qi, LIU Ya-lan, YANG Da-wei, YAN Yong-de, WANG Gui-ling, CHAI Zhi-fang, SHI Wei-qun. Thermodynamics and kinetics properties of lanthanides (La, Ce, Pr, Nd) on liquid bismuth electrode in LiCl−KCl molten salt [J]. Journal of the Electrochemical Society, 2020, 167(12): 122507.

[24] MATSUDA H, AYABE Y. On the theory of Randles−Sevik's cathode ray polarography [J]. Journal of Electrochemistry, Reports of the Bunsen Society for Physical Chemistry, 1955, 59(6): 494−503. (in German)

[25] TANG Hao, REN Yi-ming, WANG Shao-fei, DENG Hui, CAI Ding-zhou, SHAO Lang, ZHAO Yue, GAO Rui, YAN Yong-de, ZHANG Mi-lin. Electrochemical co-deposition of Mg−Ca alloys from KCl−$CaCl_2$−$MgCl_2$ melts [J]. Journal of the Electrochemical Society, 2015, 162(10): D520.

[26] LAITY R W, MCINTYRE J D E. Chronopotentiometric diffusion coefficients in fused salts: I. Theory [J]. Journal of the American Chemical Society, 1965, 87(17): 3806−3812.

[27] TANG H, PESIC B. Electrochemical behavior of $LaCl_3$ and morphology of La deposit on molybdenum substrate in molten LiCl−KCl eutectic salt [J]. Electrochimica Acta, 2014, 119: 120−130.

[28] LIU Zhao-ting, LU Gui-min, YU Jian-guo. Investigation on electrochemical behaviors of Ni(II) impurity in LiCl−KCl melt [J]. Separation and Purification Technology, 2021, 268: 118354.

[29] LIU Zhao-ting, LU Gui-min, YU Jian-guo. Investigation on electrochemical behaviors of $MgCl_2$ impurity in LiCl−KCl melt [J]. Journal of Electroanalytical Chemistry, 2021, 886: 115131.

[30] SCHARIFKER B, HILLS G. Theoretical and experimental studies of multiple nucleation [J]. Electrochimica Acta, 1983, 28(7): 879−889.

[31] CASTRILLEJO Y, BERMEJO M R, BARRADO E, MARTÍNEZ A M. Electrochemical behaviour of erbium in the eutectic LiCl−KCl at W and Al electrodes [J]. Electrochimica Acta, 2006, 51(10): 1941−1951.

[32] BERMEJO M R, GÓMEZ J, MEDINA J, MARTÍNEZ A M, CASTRILLEJO Y. The electrochemistry of gadolinium in the eutectic LiCl−KCl on W and Al electrodes [J]. Journal of Electroanalytical Chemistry, 2006, 588(2): 253−266.

[33] CASTRILLEJO Y, BERMEJO M R, BARRADO A I, PARDO R, BARRADO E, MARTINEZ A M. Electrochemical behaviour of dysprosium in the eutectic LiCl−KCl at W and Al electrodes [J]. Electrochimica Acta, 2005, 50(10): 2047−2057.

[34] BERMEJO M R, GOMEZ J, MARTINEZ A M, BARRADO E, CASTRILLEJO Y. Electrochemistry of terbium in the eutectic LiCl−KCl [J]. Electrochimica Acta, 2008, 53(16): 5106−5112.

[35] LIU Kui, WANG Wei, MA Yue, KANG Ming-liang, WANG Biao. Electrochemical properties and nucleation morphology of yttrium on tungsten substrate in molten salt [J]. Journal of the Electrochemical Society, 2020, 167(11): 112508.

[36] TYLKA M M, WILLIT J L, WILLIAMSON M A. Electrochemical nucleation and growth of uranium and plutonium from molten salts [J]. Journal of the Electrochemical Society, 2017, 164(8): H5327.

[37] TANG Hao, YAN Yong-de, ZHANG Mi-lin, LI Xing, HAN Wei, XUE Yun, ZHANG Zhi-jian, HE Hui. Fabrication of Mg−Pr and Mg−Li−Pr alloys by electrochemical co-reduction from their molten chlorides [J]. Electrochimica Acta, 2013, 107: 209−215.

$SrCl_2$−KCl−$MgCl_2$ 熔体中氯化镁的电化学行为和镁锶共沉积机理

赵 佳[1,2,3]，闫艺航[3]，张 皓[3]，高华阳[3]，张 烨[1,2,3]，路贵民[1,2]

1. 华东理工大学 国家盐湖资源综合利用工程技术研究中心，上海 200237；
2. 华东理工大学 钾锂战略资源国际联合实验室，上海 200237；
3. 华东理工大学 化工学院，上海 200237

摘 要：采用循环伏安法、方波伏安法、开路电位等电化学手段评估 $SrCl_2$−KCl 共晶体系中 $MgCl_2$ 的电化学行为和 Mg、Sr 共沉积机理。在 $SrCl_2$−KCl 体系中，Mg(II)在钨电极的还原属于一步两电子的准可逆过程；Mg、Sr 的电化学共沉积过程形成两种 Mg−Sr 金属间化合物。基于计时电流法探索共沉积过程的成核类型随过电位的演变关系，结果显示，电极表面的成核模式依赖于基体材料和电极反应产物。所有过电位下对应的前期成核归因于 Mg(II)的还原。当 Mg 和 Sr 共同沉积时，首先是 Mg(II)在电极表面还原，形成 Mg 核，随后同时进行 Sr(II)在 Mg 表面欠电位沉积和 Mg 的沉积。此外，随着 $SrCl_2$−KCl 体系中 $MgCl_2$ 浓度的增加，Mg−Sr 共沉积过程中的电流密度相应增加。

关键词：氯化镁；电化学行为；扩散系数；成核机理；共沉积

(Edited by Bing YANG)